Reconstruction of the electric field in type-II superconducting thin films in perpendicular geometry

C. Romero-Salazar* and Ch. Jooss†
Institut für Materialphysik, Friedrich Hund Platz 1, 37077 Göttingen, Germany

O. A. Hernández-Flores
Escuela de Ciencias, Universidad Autónoma "Benito Juárez" de Oaxaca, Av. Universidad s/n, Ex Hacienda Cinco Señores, Oaxaca de Juárez, Oaxaca CP 68120 México

(Received 24 November 2009; published 15 April 2010)

The study of electric field distributions induced by flux creep in type-II superconducting films allows for important insight into the mechanism of vortex dynamics, the temporal evolution of flux and current distributions, and the occurrence of local losses. Most studies are based on the assumption that a phenomenological materials law, which has been extracted from macroscopic transport measurements, can be also applied to the local electric field during magnetization decay. We evaluate this ansatz by reconstructing the three-dimensional-induced $\mathbf{E}_i$ and potential $\mathbf{E}_p$ electric fields from experimentally measured time dependence of the flux density distribution. The results are quantitatively compared with solutions of the nonlinear and nonlocal equation of motion for the flux penetration, where the Maxwell equations as well as a materials law are utilized to obtain a two-dimensional $\mathbf{E}_{i,2D}$ and $\mathbf{E}_{p,2D}$. We focus our analysis on the electric field distributions on a partially penetrated magnetized state of an epitaxial $YBa_2Cu_3O_{6.95}$ film.

DOI: 10.1103/PhysRevB.81.144506 PACS number(s): 74.20.De, 74.25.Ha, 74.25.Uv, 74.72.−h

I. INTRODUCTION

The study of vortex electrodynamics in thin-film superconductors, subjected to external magnetic fields, is an important and challenging problem for the development of high-current carrying applications with low electromagnetic losses.[1] In type-II superconductors, the electric field $\mathbf{E}$ which is related to electromagnetic losses is generated by current-induced motion or thermally activated creep of Abrikosov vortices. Microscopically, the total electric field of a moving vortex has two different origins.[2,3] It is composed by an electric field component $\mathbf{e}_i(\mathbf{r})$ which is induced by the temporal variation in the microscopic flux density $\mathbf{b}(\mathbf{r})$ according to the Faraday law $\nabla \times \mathbf{e}_i(\mathbf{r}) = -\dot{\mathbf{b}}$. In addition, the moving vortex creates a potential electric field component due to an electric displacement charge density $n^{in}(\mathbf{r})$ induced by the redistribution of the quasiparticles in the vortex core. This potential component of the electric field $\mathbf{e}_p(\mathbf{r})$ is given by $\nabla \cdot \mathbf{e}_p(\mathbf{r}) = n^{in}(\mathbf{r})/\epsilon_0$. According to the Helmholtz decomposition,[4] both electric field components contribute independently to the total electric field. In addition, a hydrodynamic contribution to the potential electric field, which was originally suggested by London,[5] has been discussed.[6]

Experimental and many of the theoretical investigations of electric field distributions consider coarse-grained electric field distributions $\mathbf{E}(\mathbf{r})$ which are obtained by spatially averaging the microscopic electric fields over the discrete vortex structure, i.e., a length scale larger than the average vortex-vortex distance. However, one should be aware that different measurement techniques may record only characteristic contributions to the total electric field $\mathbf{E}(\mathbf{r})$. Space-resolved magneto-optical (MO) imaging of the time evolution of the magnetic-flux density distribution $\mathbf{B}(\mathbf{r})$ combined with numerical methods for inversion of the Faraday law yield coarse-grained distributions of the inductive electric field component in high-temperature superconducting (HTS) thin films while the reconstruction of the potential electric field requires additional assumptions, Fig. 1.[7] In contrast, transport measurements reveal a potential drop at the electrodes being converted into an electric field by dividing through the

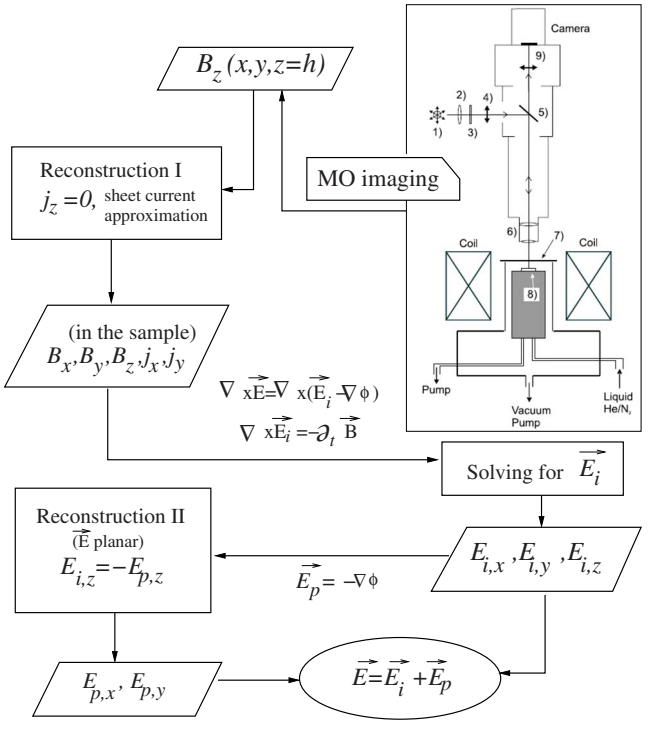

FIG. 1. (Color online) Flux diagram for the electric field $\mathbf{E}$ reconstruction from magneto-optical measurement of the time evolution of the magnetic-flux density. The measurement height for the $B_z(x,y)$ distribution is denoted by h. All other symbols are introduced in the main text.

 ©2010 The American Physical Society

electrode distance. Such measurements thus yield a potential electric field, representing an average over large regions or the entire sample. Such a procedure gives rise to a phenomenological description of the dissipative processes of the moving vortex ensemble by means of an effective material law $\mathbf{E}(j,B,T)=\rho(j,B,T)\mathbf{j}$. To some extent, this phenomenological law allows an analysis of the dissipation mechanisms by means of a flux creep or flux flow resistivity $\rho(j,B,T)$. It represents a rank two tensor and describes nonlinear transport properties in the superconducting state without going into details of both, microscopic vortex dynamics and microscopic structure of the superconducting material.[8] There are a large number of studies of $\rho(j,B,T)$ in various superconductors with different vortex-pinning potential and microstructure, showing a rich phenomenology (see, e.g., Refs. 9 and 10). Below the critical current density j_c, the dependence of the electric field on the current density is usually approximated as a power law

$$E(j) = E_c\left(\frac{j}{j_c}\right)^n = \rho(j)j. \tag{1}$$

It is used for the theoretical calculation of electric field distributions for a large variety of problems, such as the transport current in superconducting plates with various geometries.[11,12]

The effective materials law ansatz derived from transport experiments was then also successfully applied to the theoretical study of flux dynamics and time evolution of magnetization decay in superconductors. Assuming that a unique current-voltage relation can be locally applied at all regions of the sample, it allows for closing and thus solving the system of Maxwell equations. The time evolution of the flux density, current density, and electric field during magnetization relaxation was studied, depending on the external magnetic field $\mathbf{H}_a$ direction and one-dimensional or two-dimensional (2D) geometries, i.e., strips, disks, cylinders, and thin plates.[13–16] In the flux creep regime, an universal behavior of the electric field distribution during flux creep is revealed. This means that some transient time after the ramp of $\mathbf{H}_a$ is stopped, the relaxing $E(\mathbf{r},t)$ separates into a universal spatial profile $f(\mathbf{r})$ and a time dependence $g(t)\approx 1/t$. All the 2D electric field calculations assume zero thickness and consider a 2D sheet current density.[14] An experimental study of the electric field during magnetization decay was performed in HTS single crystals by Giller *et al.*,[17] where $\mathbf{E}_i$ was determined from the time evolution of the flux density. Analyzing the local time dependence of a magnetization current by time-resolved and spatially resolved magneto-optical technique, a nonconstant spatial distribution of the local activation energy $U_0(x,y)$ was found in a homogeneous thin film,[18] indicating that local relaxation behavior may strongly depend on geometry.

In spite of the great success of this theoretical work to reproduce experimentally observed flux and current distributions in various geometries and conditions,[19,20] one should be aware that all materials laws such as the power ansatz are extracted from macroscopic experiments. Strong local variations in the *E-j* relation may be due to flux density gradients, vortex phase transitions,[17] charging at current domain boundaries[7] or geometric reasons such as holes or hole arrays.[21] In addition to such geometrical effects, anisotropic current densities may arise even in isotropic superconductors due to flux Hall effects or vortex dragging.[8] Consequently, the application of the condition $\mathbf{E}\|\mathbf{j}$ may not be generally justified. We give evidence in this paper that at current domain boundaries or inhomogeneities, not only Lorentz and pinning forces play a role in the resultant direction of the flux-line motion but the effect of hydrodynamic (Magnus) and Hall forces cannot be disregarded. Such studies require further progress in determining local electric field distributions which are not based on a material law ansatz.

In this contribution, we present an experimental and theoretical study of potential and inductive electric field components in a homogeneous superconducting film with finite thickness. We restrict this paper to the problem of flux creep in the so-called *perpendicular geometry*, that is, we study the thermally activated vortex motion in superconducting thin films subjected to an external magnetic field $\mathbf{H}_a$, perpendicular to the sample surface. Our aim is to develop a consistent technique to distinguish between the two contributions to the electric field, the induced $\mathbf{E}_i$ and the potential component $\mathbf{E}_p$. The $\mathbf{E}_i(x,y,z)$ distributions are reconstructed via magneto-optical imaging and the Faraday's law as described in a previous paper.[7] The main step of this paper represents the determination of the $\mathbf{E}_p(x,y,z)$ distribution beyond the assumption of $\mathbf{E}\|\mathbf{j}$, used in Ref. 7 ($\mathbf{E}=\mathbf{E}_i+\mathbf{E}_p$). Our new and more general approach only requires a symmetry argument on the boundary conditions at the surfaces which guarantee charge neutrality of the total sample and that the total electric field $\mathbf{E}_i+\mathbf{E}_p$ lies in the *x-y* plane of the superconducting film. A planar total electric field is fully consistent with the presence of a planar current density in thin films with thickness $d<\lambda$ in perpendicular external field, where λ is the magnetic penetration depth. The planar current density $\mathbf{j}(x,y)=j_x(x,y)\mathbf{e_x}+j_y(x,y)\mathbf{e_y}$ is assumed to neither have a j_z component nor to posses a z dependence of the planar components. In contrast, all three vector components of $\mathbf{B}(\mathbf{r})$, $\mathbf{E}_i(\mathbf{r})$, and $\mathbf{E}_p(\mathbf{r})$ are calculated in the three-dimensional (3D) space because they vary strongly within a thin superconducting film as well as in the exterior. We therefore consider our theoretical approach as quasi-3D. It will turn out that the electric field components $E_{p,z}(x,y)=-E_{i,z}(x,y)$ perpendicular to the current density are the key to obtain the electrostatic potential and electric charge density induced by flux creep. In fact, $E_z=E_{p,z}+E_{i,z}=0$ is valid in the quasistationary state, where the (fast) process of induced charge generation perpendicular to the film plane is controlled by the slow process of magnetic relaxation due to flux creep. $E_z=0$ and thus $E_{p,z}(x,y)=-E_{i,z}(x,y)$ due to the induced surface charges is in full agreement with $j_z=0$ (see Fig. 2). In extension of Ref. 7 this guarantees $\nabla\times\mathbf{E}_p(\mathbf{r})=0$ at the current domain boundaries. As a consequence, at the domain boundaries, the total electric field is not directed parallel to the current.

In order to compare reconstructed electric fields from experiments with theoretically simulated results based on an isotropic materials law, we employ a power-law ansatz to close the Maxwell equations for the time evolution of the 2D sheet current. The obtained total electric field is decomposed in $\mathbf{E}_i$ and $\mathbf{E}_p$ components via Helmholtz decomposition. This

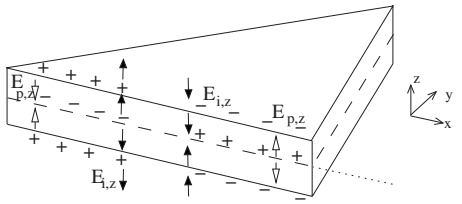

FIG. 2. Scheme of the induced charge distribution in a superconducting thin film. Only the sign of the surface charge density at the $z=\pm\delta$ planes and the bulk charge density at the $z=0$ plane are shown. They are the source of the z component of the potential electric field $E_{p,z}$. In the quasistationary state, $E_{p,z}=-E_{i,z}$ and thus $j_z=0$.

gives rise to the following outline of the paper: Sec. II presents the theoretical scheme to calculate the induced electric field and reconstruct the potential electric field from experimental data. Section III presents experimental results based on time- and space-resolved magneto-optical imaging and electric field reconstruction for a magnetized YBaCuO square-shaped thin film in partly penetrated state. In addition, the electric field results from numerical simulations based on the power-law ansatz are presented, considering a sample of finite thickness and an ideal two-dimensional sample. Section IV compares theoretical predictions and experimental distributions and analyze physical impact of the generalized electric field reconstruction. Finally, Sec. V summarizes our results.

II. THEORY

The study of electric field distribution for flux creep in a type-II superconducting thin plate is based on the Maxwell equations for a material with mesoscopic, coarse-grained electric and magnetic fields on a length scale ($\approx 1\ \mu$m). This corresponds to an average over many vortices and over distances larger than the characteristic distance of pinning sites. The set of equations is given by

$$\nabla \times \mathbf{H} = \mathbf{j} + \frac{\partial \mathbf{D}}{\partial \mathbf{t}}, \tag{2}$$

$$\nabla \cdot \mathbf{B} = \mathbf{0}, \tag{3}$$

$$-\nabla \times \mathbf{E} = \dot{\mathbf{B}}, \tag{4}$$

$$\epsilon_0 \nabla \cdot \mathbf{D} = n^{ex}. \tag{5}$$

In the quasistationary limit, the temporal derivative of D is much smaller than the temporal evolution of the current density, and, in the following is thus disregarded. Since we consider an electrically insulated sample, $n^{ex}=0$ and Eq. (5) can be simplified to $\epsilon_0 \nabla \cdot \mathbf{E_p} = n^{in}$, where n^{in} represents the induced charge density.

Helmholtz's decomposition represents a natural way to find a solution for the pair of Eqs. (4) and (5). Specifically, Helmholtz's theorem[4] can be applied to our electromagnetic boundary problem. Indeed, the electric field $\mathbf{E}$ can be completely and uniquely decomposed into a sum of the induced electric field $\mathbf{E}_i$ plus the electrostatic potential field $\mathbf{E}_p$ with appropriate boundary conditions. In general, the induced and potential electric fields obey the following relations:

$$\nabla \times \mathbf{E}_i = -\dot{\mathbf{B}}, \tag{6}$$

$$\nabla \cdot \mathbf{E}_i = \mathbf{0}, \tag{7}$$

$$\epsilon_0 \nabla \cdot \mathbf{E}_p = n^{in}, \tag{8}$$

$$\nabla \times \mathbf{E}_p = \mathbf{0}. \tag{9}$$

Knowing the magnetic induction $\mathbf{B}$ as much as the planar current density $\mathbf{j}(x,y)=j_x(x,y)\mathbf{e_x}+j_y(x,y)\mathbf{e_y}$ circulating in the x-y plane the electric field can be reconstructed. The method is based on inversion of Biot-Savar's law to determine $\mathbf{j}(x,y)$ from the measured $B_z(x,y)$, application of Biot-Savart's law in forward direction, in order to determine all three vector components $\mathbf{B}(x,y,z)$ in the entire space and using Faraday's law to determine $\mathbf{E}_i(x,y,z)$ as described in Ref. 7.

The integral version of the Faraday equation for the induced electric field is given by

$$\mathbf{E}_i = \frac{1}{4\pi} \nabla \times \int \frac{\dot{\mathbf{B}}}{R} dV', \tag{10}$$

where dV means integration over infinite space unless stated otherwise.

For a thin film of arbitrary shape a 2D Fourier transformation

$$\tilde{f}(k_x,k_y) = \int_{-\infty}^{\infty} dx \int_{-\infty}^{\infty} dy f(x,y) f^{i(k_x x + k_y y)} \tag{11}$$

can be applied in the (x,y) plane to perform the integration. A sufficiently large outer space avoids influencing the results by periodic continuation. For half thickness δ smaller than $1/k_{\max}$ the Fourier components of the in-plane-induced electric field are given by

$$\tilde{E}_{i,x}(k_x,k_y,z=0) = \frac{\mu_0}{2k^3}\{\dot{\alpha}k_y\}(k\delta), \tag{12}$$

$$\tilde{E}_{i,y}(k_x,k_y,z=0) = -\frac{\mu_0}{2k^3}\{\dot{\alpha}k_x\}(k\delta), \tag{13}$$

where $k=|\mathbf{k}|=\sqrt{k_x^2+k_y^2}$, $\delta=d/2$, and $\dot{\alpha}=(k_y\partial_t\tilde{j}_x-k_x\partial_t\tilde{j}_y)/k$.

The system conformed by the Eqs. (6) and (8) would be a complete system of equations including solutions for the potential electric field, if the induced charge density n^{in} is known. The studied thin-film geometry, however, allows for a complete reconstruction of the electric field in the quasistationary state. For such a slowly relaxing magnetization decay in a superconducting thin film, the induced charge density is mainly located at the boundaries. For film thickness $d \ll a$, where a represents the lateral dimension of the sample, the dominating contribution comes from the $z=\pm\delta$ planes. It is built up by a perpendicular displacement current $j_z(x,y,t)$ due to the perpendicular induced field component

$E_{z,i}(\mathbf{r})$. The latter is generated by temporally changing in-plane components of the magnetic induction $B_x(\mathbf{r})$ and $B_y(\mathbf{r})$. Considering hypothetically a short and quick temporal variation in the flux: the induced displacement current component $j_z(\mathbf{r})$ ($|z| \leq \delta$) which is present due to the $E_{i,z}(x,y)$ component, quickly drops down to zero after a transient time because of the built up of induced surface charges at $z = \pm d/2$ and the related counter field $E_{p,z}(\mathbf{r})$. This exactly defines the quasistationary state, where the flux dynamics is slow enough to establish a situation, where the $E_{i,z}$ component generated by relaxation of in-plane flux components is exactly compensated by $E_{p,z}(x,y) = -E_{i,z}(x,y)$ due to the induced surface charge at the planes and thus $j_z = 0$. The condition of quasistationarity consequently agrees with the condition of a planar **j** and that the total electric field **E** is planar.

A. Reconstruction of $\mathbf{E}_p$ from E_{iz}

Naturally, the z-component $E_{i,z}$ of the induced electric field is required to reconstruct the induced surface charge density, and, what will be shown below, all three vector components of the potential electric field $\mathbf{E_p}$. The 2D Fourier representation of the z component of the induced electric field, Eq. (10), is [see Eq. (20) in Ref. 7),

$$\tilde{E}_{i,z} = \frac{i\mu_0}{4k}\dot{\beta}\int_{-\infty}^{+\infty} dz' e^{-k|z-z'|}\{e^{-k|z'-\delta|} - e^{-k|z'+\delta|}\}, \quad (14)$$

where $\dot{\beta} = (\mathbf{k}\cdot\partial_t\tilde{\mathbf{j}})/k$ can be associated with the identity $(k_x\partial_t\tilde{j}_x + k_y\partial_t\tilde{j}_y)k^{-1} = -\partial_z/k\partial_t\tilde{j}_z - \partial_t^2 n^{in} \neq 0$. This reflects the temporal variation in the displacement current density which would be present after a sudden flux relaxation step and builds up the induced surface charge before reaching the quasistationary limit. It is thus well suited to calculate $E_{i,z}$. However, for the quasistationary state $E_{p,z}(x,y) = -E_{i,z}(x,y)$, no real j_z is flowing as discussed above. Once the integration, Eq. (14), is performed, the final expression for $\tilde{E}_{i,z}$ is

$$\tilde{E}_{i,z} = \frac{i\mu_0}{4k^2}\dot{\beta}e^{-k\delta}\{D\sinh(kz) - 2kz\cosh(kz)\}, \quad (15)$$

where $D = 2k\delta + 2$.

To reconstruct the potential electric field $\mathbf{E}_p$, we start considering its irrotationality $\nabla \times \mathbf{E}_p = 0$. The components of such a vector identity provides us with an homogeneous system of partial differential equations. As we emphasized, since the total electric field **E** must lie in the x-y plane, one has also to take into account here that $E_{i,z} = -E_{p,z}$. With this relation, the system of equations is nicely decoupled and, in the 2D Fourier (k_x, k_y) space, acquires the form

$$ik_y\tilde{E}_{p,z} - \partial_z\tilde{E}_{p,y} = 0, \quad (16)$$

$$\partial_z\tilde{E}_{p,x} - ik_x\tilde{E}_{p,z} = 0, \quad (17)$$

$$ik_x\tilde{E}_{p,y} - ik_y\tilde{E}_{p,x} = 0. \quad (18)$$

It is easy to show that the third equation is a consequence of the first two equations. Consequently, one has a two *independent* first-order ordinary differential equations, however, Eq. (18) comes into play for the determination of the integration constant. Integrating over the z component, one yields

$$\tilde{E}_{p,x} = -ik_x\int \tilde{E}_{i,z}dz + C_x, \quad (19)$$

$$\tilde{E}_{p,y} = -ik_y\int \tilde{E}_{i,z}dz + C_y. \quad (20)$$

Without loss of generality, one can write the integration constants as $C_x = -ik_xC$ and $C_y = -ik_yC$, which, in fact fulfill Eq. (18). If we define

$$\tilde{\phi} = \int \tilde{E}_{i,z}dz + C, \quad (21)$$

and conclude straightforwardly that $\tilde{\phi}$ is the two-dimensional Fourier transformation of the scalar potential ϕ. Therefore, the potential electric field $\mathbf{E}_p$ is determined up to a integration constant C, which depends on the boundary conditions of the particular system under study. Since a moving vortex medium is characterized by a polarization vector field, then, although an isolated superconductor is a neutrally charged body, there is a nonzero-induced electrical charge density defined as $n^{in} = \epsilon_0\nabla\cdot\mathbf{E}_p$. The induced charge density in the 2D Fourier space can be written as

$$\frac{\tilde{n}^{in}}{\epsilon_0} = k^2\tilde{\phi} - \partial_z\tilde{E}_{i,z}, \quad (22)$$

where $\partial_z\tilde{E}_{i,z}$ is given by the Eq. (15).

The solution does not fulfill the condition of uniqueness due to the integration constant C. However, employing physical arguments, a suitable solution for $\mathbf{E}_p$ can be established. The most general boundary condition for C is that the volume integral over n^{in} plus the surface integral over the surface charge density σ^{in} must vanish and consequently the total superconducting sample is charge neutral. However, this integral equation is not sufficient to derive an equation to determine C. Consequently, we apply an additional symmetry argument. In a 2D model of a superconducting plate, the integral over the induced surface charge density and the bulk charge density would collapse into a condition of local zero charge at every position in the (x,y) plane. The correspondence to the quasi-3D model can be used to derive a symmetry argument for the unknown bulk charge density $n^{in}(x,y,z)$ in the superconducting film. Using the $z=0$ plane as a symmetry plane of the problem, it follows from the antisymmetry of $E_{i,z}$ and $E_{p,z}$ with respect to $z=0$ (Fig. 2 in the paper) that $\sigma^{in}(x,y,z=+\delta) = \sigma^{in}(x,y,z=-\delta)$ for any (x,y). This step just follows from the sample geometry and does not represent an additional assumption. Applying the condition of zero local charge at any point of the (x,y) to the quasi-3D case, one gets an expression of the bulk charge density at the $z=0$ plane

$$n^{in}(z=0)d = b\cdot\sigma^{in}(z = \pm\delta), \quad (23)$$

where the parameter b depends on the charge-density distribution along the z axis. This equation does still not allow for

calculating the z dependence of $n^{in}(x,y,z)$. In order to solve the problem for the $z=0$ plane, we have assumed that the surface charge is fully compensated by the volume charge $n^{in}(x,y,z=0)d$ which is mathematically expressed by the integer value −2. In this case the charge density at the central plane is $n^{in}(x,y,z=0)d=-0.5\sigma^{in}(x,y,z=\pm\delta)$. The induced surface charge at the lateral sample edges $\sigma^{in}(\pm a,y,z)$ and $\sigma^{in}(x,\pm a,z)$ is disregarded in the further calculations. The lateral surfaces are a/d times smaller than the top surfaces of the sample. Consequently, their contributions are small and restricted to a very narrow edge area of a width on the order of d. This is below the spatial resolution of the experiments. Equation (23) is then further used to adjust the integration constant C and for the two components $\tilde{E}_{p,x}$ and $\tilde{E}_{p,y}$ of the potential electric field at the $z=0$ plane in 2D Fourier space follows,

$$\tilde{E}_{p,x}(k_x,k_y,z=0)=\frac{k_x}{2}\frac{\mu_0}{k^3}\dot{\beta}\left\{1+\frac{2b-1}{1-b}(k\delta)\right\}(k\delta), \quad (24)$$

$$\tilde{E}_{p,y}(k_x,k_y,z=0)=\frac{k_y}{2}\frac{\mu_0}{k^3}\dot{\beta}\left\{1+\frac{2b-1}{1-b}(k\delta)\right\}(k\delta). \quad (25)$$

Here again, we have considered the approximation $k\delta \ll 1$. Note that the potential electric field has a term proportional to $(k\delta)$, like the induced electric field, plus a term proportional to $(k\delta)^2$.

B. Electric fields from flux simulations

The numerical simulation of the time evolution of the flux and sheet current are performed similar to the scheme published by Brandt[14] based on a potential law ansatz for the scalar flux creep resistivity. In order to calculate the resulting induced electric field, the Faraday equation is solved relating $\mathbf{E}_i$ to the temporal evolution of the current distribution in a film of finite thickness. The Eq. (10) can be then rewritten as follows:

$$\mathbf{E}_i=\mu_0\int_V\frac{\partial_t\mathbf{j}}{4\pi R}dV'+\oint_S\frac{\partial_t\mathbf{B}\times\hat{\mathbf{n}}}{4\pi R}dS'.$$

We restrict our attention to the plane $z=0$ of a square film with width a and thickness $d=2\delta$. The original 3D calculation can then be restricted to the integral

$$\mathbf{E}_i(x,y,z=0)=\mu_0\frac{\delta}{a}\int_{-a/2}^{+a/2}\int_{-a/2}^{+a/2}\partial_t\mathbf{J}Kdx'dy', \quad (26)$$

where the kernel K is given by

$$K=\ln\left\{\frac{+\delta+\sqrt{(x-x')^2+(y-y')^2+\delta^2}}{-\delta+\sqrt{(x-x')^2+(y-y')^2+\delta^2}}\right\}-\frac{2a}{\sqrt{(x-x')^2+(y-y')^2+\delta^2}}.$$

Note that the Eq. (26) is obtained for the sheet current $\mathbf{J}$ by $\mathbf{J}(x,y)=d\mathbf{j}(x,y)$.[13,14] Because the $\mathbf{J}$ calculation requires the current-voltage relation (1), Eq. (26) is solved numerically.

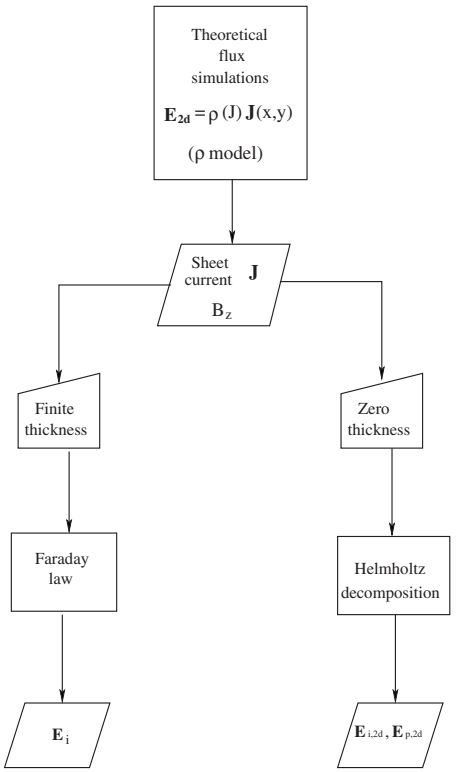

FIG. 3. Flux diagram describing how the induced $\mathbf{E}_{i,2D}$ and potential $\mathbf{E}_{p,2D}$ electric field components are obtained via magnetic flux simulations.

In addition to the calculation of the induced electric field in square geometry with finite thickness, we apply the Helmholtz decomposition of the electric field for the electric field distribution directly calculated from the materials law in an infinitesimal thin film. Again, a method based on Brandt's scheme[13,14] for the flux and electric field simulations is applied. The Helmholtz decomposition divides the electric field $\mathbf{E}_{2D}$ into the sum of a potential field (irrotational) $\mathbf{E}_{p,2D}$ and an induced (soleinodal) $\mathbf{E}_{i,2D}$ field. For the electric field decomposition, we will follow the Gui and Dou[22] procedure. The two-dimensional electric field $\mathbf{E}_{2D}(x,y)=E_{x,2D}(x,y)\hat{\mathbf{x}}+E_{y,2D}(x,y)\hat{\mathbf{y}}$ can be obtained performing the transformation $\mathbf{E}_{2D}=-\nabla^2\mathbf{W}$, where the vectorial function $\mathbf{W}$ is a first order and continuously differentiable function. Each component of the last expression represents a two-dimensional Poisson equation whose uniqueness depends on application of appropriate boundary conditions. We are interested in the electric field within the sample with is bounded by the surface S.

$$\mathbf{W}=\frac{1}{2\pi}\int_{-a}^{a}\int_{-a}^{a}\mathbf{E}_{2D}\ln\frac{1}{\sqrt{(x-x')^2+(y-y')^2}}dx'dy'. \quad (27)$$

Using the vector identity $\nabla^2\mathbf{W}=\nabla(\nabla\cdot\mathbf{W})-\nabla\times(\nabla\times\mathbf{W})$, one can identify both the induced electric field and the electrostatic potential as $\mathbf{E}_{i,2D}=\nabla\times(\nabla\times\mathbf{W})$, and $\mathbf{E}_{p,2D}=-\nabla(\nabla\cdot\mathbf{W})$. Consequently, making use of the sheet current $\mathbf{J}(x,y)$, Eq. (27) is numerically integrated by Gaussian-Legendre quadratures. In Fig. 3, the steps to calculate the

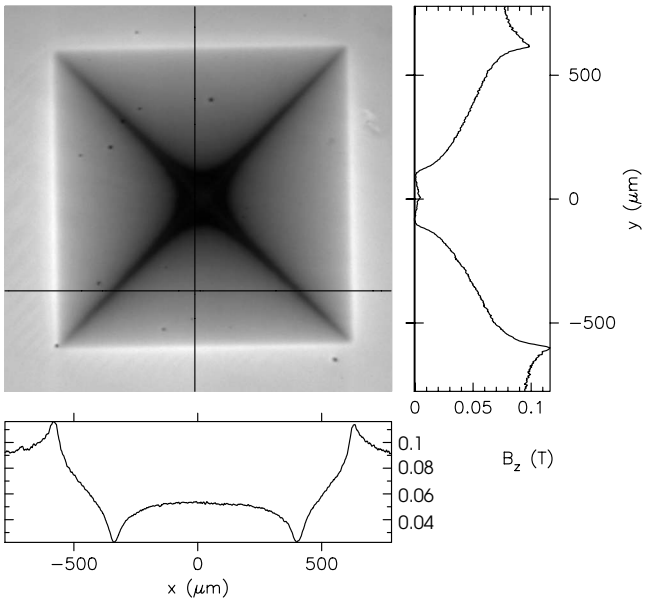

FIG. 4. Calibrated magneto-optical image showing the B_z magnetic induction distribution of a square-shaped YBaCuO film as a gray-scale image. The thin film has a thickness $d=500$ nm and width $a=1.2$ mm. The image is taken 0.731 s after ramping up the external field from a zero-field-cooled state at $T=8$ K to $\mu_0 H_a = 86$ mT.

electric field $\mathbf{E}_{2D}(x,y)$ via magnetic-flux simulations based on a material law is summarized.

III. RESULTS

In this section, we present the electric field distributions obtained by the methods presented in the former section. Our sample is a nearly single-crystalline $YBa_2Cu_3O_{6.95}$ (YBaCuO) film, grown by pulse laser deposition. The square-shaped YBaCuO film has a thickness $d=500$ nm and a width $a=1.2$ mm. After zero-field cooling to $T=8$ K, an external magnetic field $\mu_0 H_a=86$ mT was applied with a ramp rate of 0.3 mT/s. A series of images, with a time resolution of 120 ms, of the normal component of the magnetic induction B_z, were taken after the external magnetic field is kept constant. The images are in magnetic relaxation regime and in partly penetrated state. The measured light intensities are calibrated into flux densities as described in Ref. 23. Figure 4 depicts the highly homogeneous $B_z(x,y)$ distribution at $t=0.731$ s after the external ramp rate was stopped.

First, we present the reconstruction of the $\mathbf{E}_i$ and $\mathbf{E}_p$ fields from magneto-optical imaging. The resulting inductive electric field distributions $E_{i,x}(x,y)$ and $E_{i,y}(x,y)$, at $t=0.731$ s after the external magnetic field $\mathbf{H}_a$ sweep, are visualized in the panels (a) and (b) of Fig. 5, respectively. They were obtained after a back fast-Fourier transformation of the Eqs. (12) and (13). One can observe the same features of the corresponding distributions, $E_{i,x}(x,y)$ and $E_{i,y}(x,y)$, presented in Ref. 7 (compare with Fig. 11). The slight asymmetry of the experimental $E_{i,x}(x,y)$ and $E_{i,y}(x,y)$ distributions comes from the finite measurement accuracy for $B_z(x,y,t)$ in MO measurements. Even very small measurement errors in the order of 0.5% over the entire (x,y) plane may give rise to a significant asymmetry in the induced electric field because of the volume integration over the temporal derivative of the flux density distribution. The components $E_{p,x}(x,y)$ and $E_{p,y}(x,y)$ of the potential electric field distribution, at the plane $z=0$, are depicted in panels (a) and (b) of Fig. 6. They were obtained after fast-Fourier backtransform of the Eqs. (24) and (25). The potential (electrostatic) field is one order of magnitude less than the induced electric field $\mathbf{E}_i$. It presents a wigglelike structure which is not related to experimental artifacts and is richer than the induced electric field distribution (compare with Fig. 5).

In order to compare the induced electric field determined from MO experiments with the results of flux simulations for the flux creep state in a superconducting thin film of finite thickness, the panels (c) and (d) of Fig. 5 depicts the induced electric field components, $E_{i,x,2D}$ and $E_{i,y,2D}$, obtained solving the Eq. (26). The sheet current has been obtained by numerical simulations based on the power law Eq. (1). The model sample has the same thickness d and width a as the experimental one. In addition the critical current density j_c and the external magnetic field value $\mu_0 H_a=86$ mT exactly meets the experimental situation. One can observe that the distributions $E_{i,x}$ and $E_{i,y}$ reproduce the main characteristics of the corresponding obtained with experimental data [compare panels (a) with (c) and (b) with (d) of Fig. 5]. Most significant differences occur at the Meissner zone, where $\mathbf{E}_i$ obtained from flux simulations is much smaller than the experimental one.

In addition, the induced $\mathbf{E}_{i,2D}$ and potential $\mathbf{E}_{p,2D}$ electric fields for a infinitesimal thin superconducting film derived from numerical simulations are shown in panels (e) and (f) of Fig. 5 and (c) and (d) of Fig. 6, respectively. The 2D sample has the same lateral extension $a=1.2$ mm of the experimental one and the same value for the external magnetic field $\mu_0 H_a=86$ mT was considered. Once the simulated magnetic induction B_z distribution is obtained, the Helmholtz decomposition of the material law is be performed. Note that the Helmholtz decomposed $\mathbf{E}_{i,2D}$ and $\mathbf{E}_{p,2D}$ are not zero in the Meissner zone (and at the exterior of the sample), in contrast to the total electric field $\mathbf{E}_{2D}$.

Let us sum up the essential features of the induced electric field $\mathbf{E}_{i,2D}$ presented in panels (e) and (f) of Fig. 5: at the nonpenetrated area, the antisymmetric $E_{i,x,2D}(x,y)$ and $E_{i,y,2D}(x,y)$ functions have a sign inversion, as the experimentally obtained $\mathbf{E}_i$ components [compare with panels (a) and (b) of the same figure]. The distributions in panels (e) and (f) have profiles in the Meissner zone more pronounced than those presented in panels (c) and (d). However, the $E_{i,x,2D}(x,y)$ and $E_{i,y,2D}(x,y)$ components, derived from the power law in the infinitely thin-film components are dominated by the y and x current domains, respectively, display a nonmonotonous behavior and a sign reversal. This can be seen, e.g., in the profiles of the $E_{i,y,2D}$ component, whereas an oscillatory behavior occurs absent in the experimentally determined $E_{i,y}$ distribution [compare panel (f) with panel (b) of Fig. 5]. Thus, the induced electric field $\mathbf{E}_{i,2D}$ derived from the power law reproduces qualitatively the main features of the experimentally determined $\mathbf{E}_i$ and has the right order of

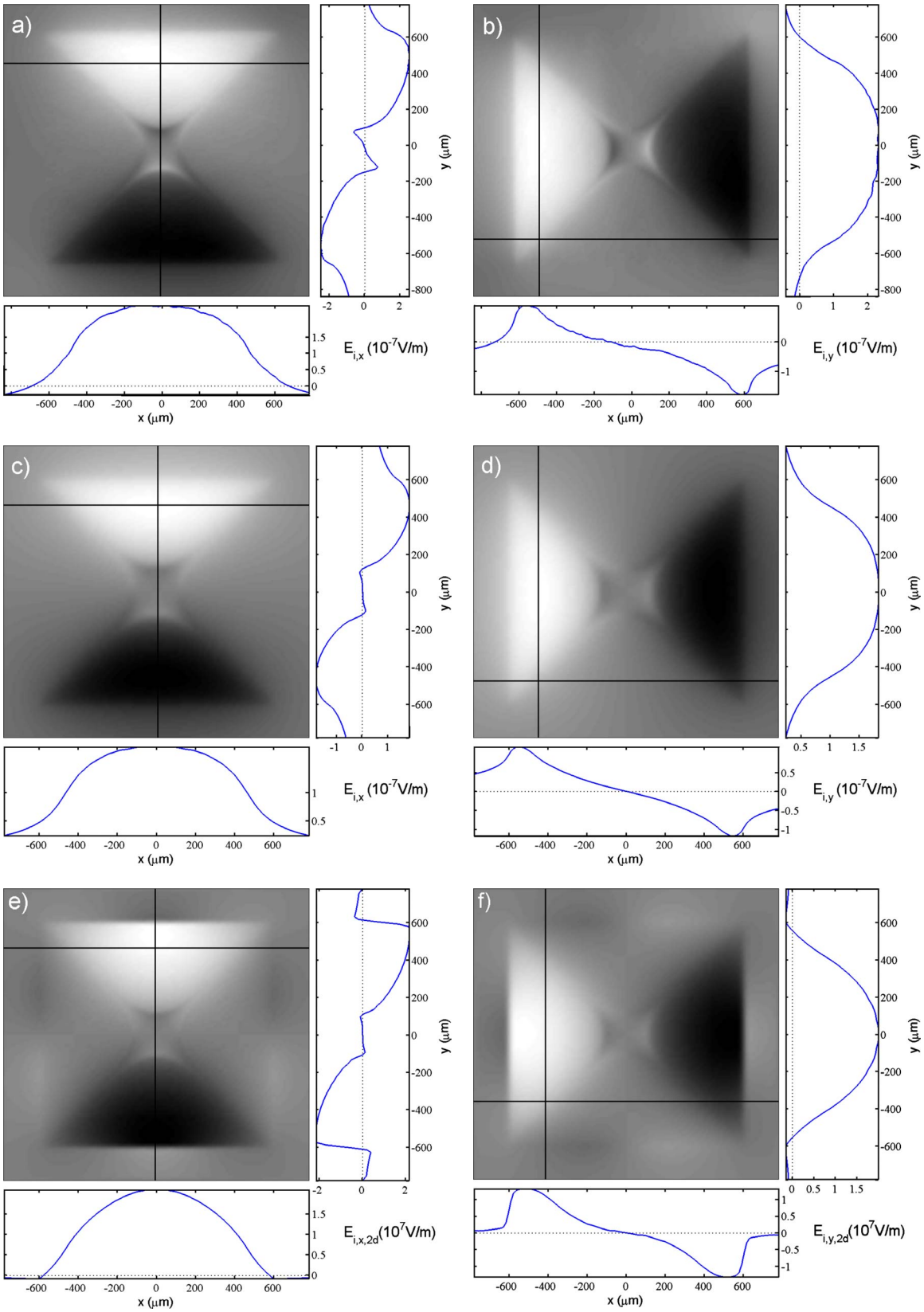

FIG. 5. (Color online) Gray-scale map of the induced electric field components calculated for three cases: (1) $E_{i,x}(x,y)$ and $E_{i,y}(x,y)$ in panels (a) and (b), respectively, were obtained from thermally activated flux creep data from the sample in Fig. 4 via the Eqs. (12) and (13); (2) $E_{i,x}(x,y)$ and $E_{i,y}(x,y)$ in panels (c) and (d), respectively, were obtained from flux simulations for a square film of finite thickness, via the Eq. (26); (3) $E_{i,x,2D}(x,y)$ and $E_{i,y,2D}(x,y)$ in panels (e) and (f), respectively, were obtained via the Helmholtz decomposition of the total electric field derived in 2D flux simulations based on the material law $\mathbf{E}_{2D}=\rho(J)(\mathbf{J})$ for an infinitely thin film.

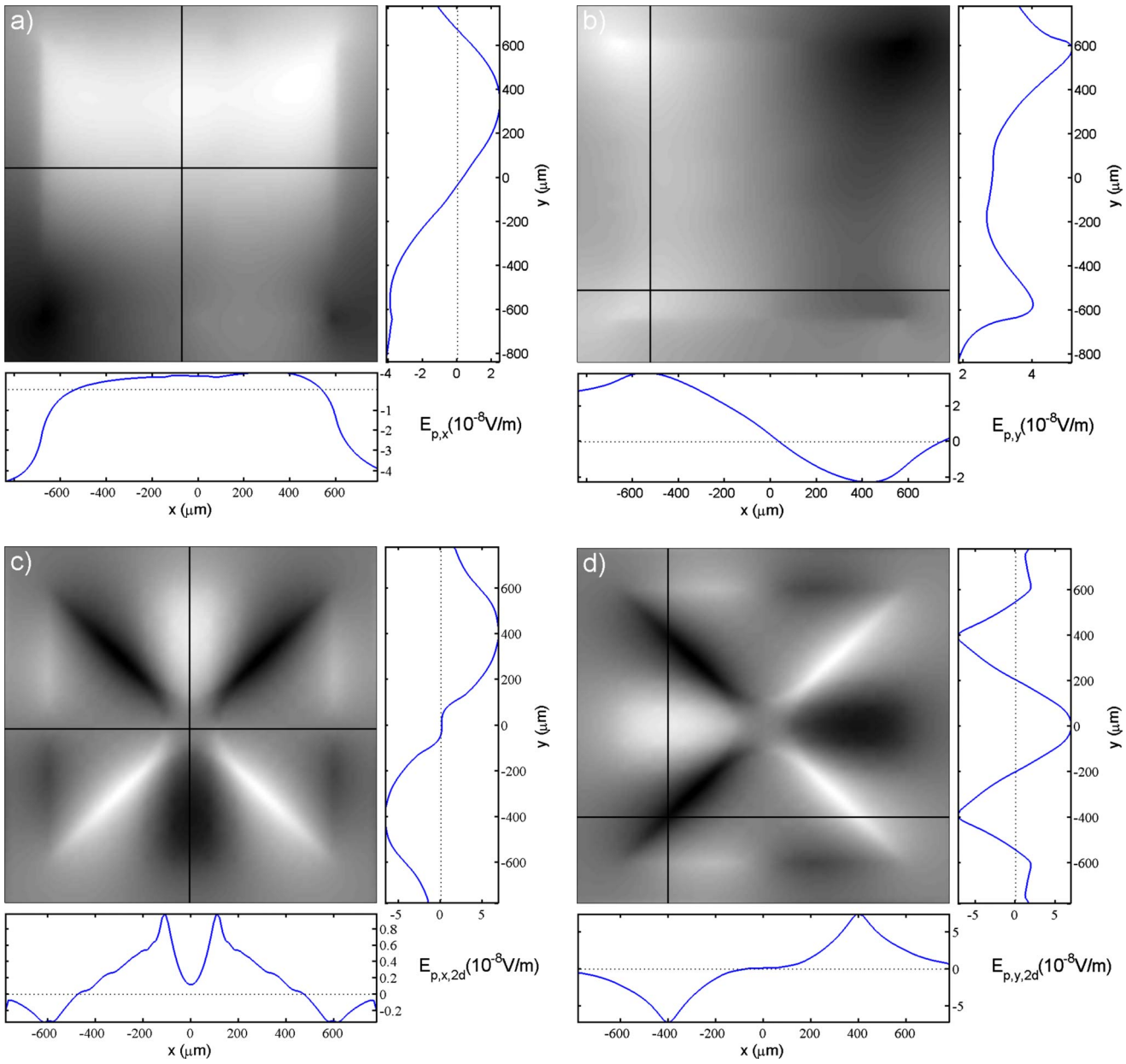

FIG. 6. (Color online) Potential electric field components: (a) $E_{p,x}$ and (b) $E_{p,y}$, obtained by a reconstruction with experimental data; (c) $\mathbf{E}_{p,x,2D}$ and (d) $\mathbf{E}_{p,y,2D}$, obtained via the Helmholtz decomposition of the material law $\mathbf{E}_{2D}=\rho(j)\mathbf{J}$.

magnitude (quantitative agreement within a factor of 2). There are significant differences in the detailed quantitative distributions and additional sign reversals which are not consistent with the result obtained from Faraday law in finite thickness.

Panels (c) and (d) of Fig. 6 show the potential field distributions $E_{p,x,2D}$ and $E_{p,y,2D}$ based on the power law in a film of finite thickness. First of all, they have opposite sign with respect to the $E_{p,x}$ and $E_{p,y}$ reconstructed from the experimental data and the current domain boundaries represent lines of symmetry [compare panels (a) with (c) and (b) with (d) in Fig. 6]. The magnitude $|\mathbf{E}_p|$ from power law presents the same maximum at each of the four current domain boundaries. In the $y(x)$ direction, the $E_{p,x,2D}(E_{p,y,2D})$ distribution has an oscillatory behavior including a sign reversal with respect to the line $y=0(x=0)$, absent in the experimentally reconstructed $E_{p,x}$ and $E_{p,y}$ distributions [e.g., compare panels (b) and (d) of Fig. 6]. Thus, the potential field distributions derived from experiment and from the numerical simulations strongly disagree.

IV. DISCUSSION

According to the Faraday law, the induced electric field is determined by the time variation in the flux density in the area enclosed by the electric field lines and thus strongly depends on the sample geometry. Comparing $\mathbf{E}_i$ in Figs. 5(a)–5(d) obtained by applying the Faraday equation to measured and simulated time-dependent flux density distributions, respectively, one may notice that they are very similar

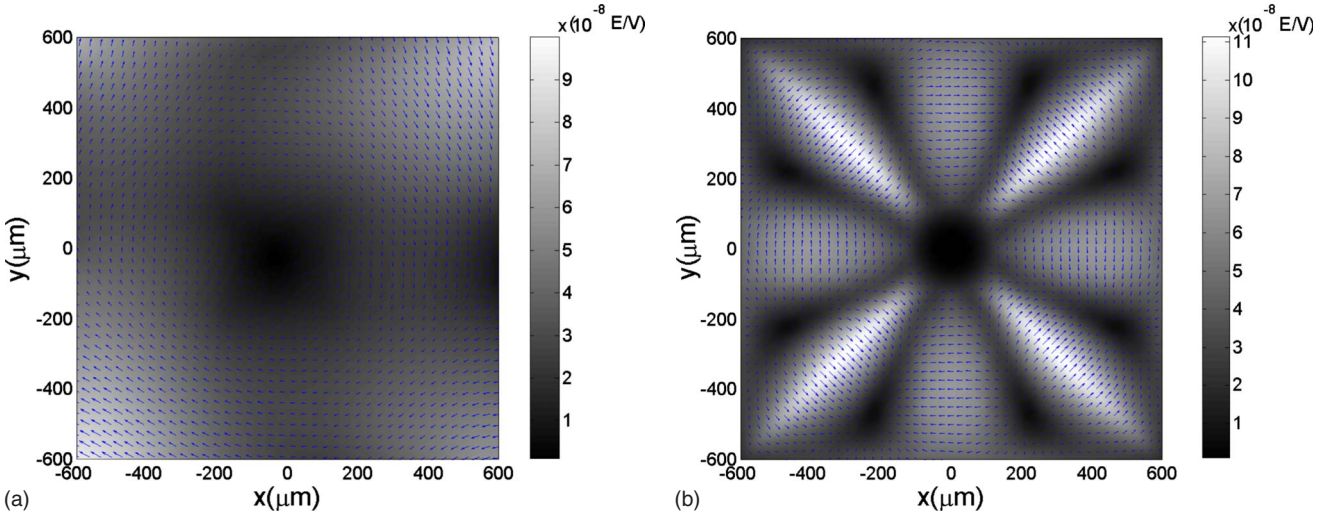

FIG. 7. (Color online) Comparison of the potential electric field distribution determined by reconstruction from experiment (a) and from 2D flux simulation based on the isotropic materials law (b). (a) $\mathbf{E}_p(x,y)$ is reconstructed from the same experimental data used for the determination of $\mathbf{E}_i$ in Figs. 5 and 6. (b) $\mathbf{E}_{p,2D}$, obtained via the Helmholtz decomposition of the total electric field $\mathbf{E}_{2D}=\rho(j)\mathbf{j}$ using a power law for $\rho(j)$. Shown are the superposition of the magnitude (gray scale) and the vector field plot of $\mathbf{E}_p$ and $\mathbf{E}_{p,2D}$, respectively.

in magnitude and symmetry. In contrast, the $\mathbf{E}_{i,2D}$ distribution obtained from Helmholtz-decomposition of the electric field [Figs. 5(e) and 5(f)] exhibits significant differences. A qualitatively new feature is an additional sign reversal of $E_{i,x,2D}$ and $E_{i,y,2D}$ in the j_y and j_x current domains, respectively, which is in contradiction to the result of Faraday law. It results from locally applying a material law obtained by macroscopic measurements of stationary transport currents to the problem of time-dependent magnetization decay. The only difference between $\mathbf{E}_i$ in Figs. 5(a)–5(d) is that the time evolution of the flux density and sheet current is either obtained from experiment or from flux simulations, respectively. Although the flux simulations are based on the local application of the materials law for the electric field, the resulting time evolution of flux density and sheet current nicely agree with the experiment. This also applies for the induced electric field $\mathbf{E}_i$, since it is determined by the Faraday law from the time evolution of the flux density in the correct geometry. This emphasizes that the determination of $\mathbf{E}_i$ in thin films represents a nonlocal problem, where the details of the sample geometry, i.e., the finite sample thickness, has to be taken into account.

The potential electric field $\mathbf{E}_p$ reconstruction emerges as an inverse problem, where the induced charge density n^{in} is an unknown quantity. Therefore, is necessary for the theoretical calculation to establish an additional condition, in order to find a solution: this is the assumption of a planar total electric field, with $E_{i,z}+E_{p,z}=0$, which is in agreement with the sheet current approximation. This can be achieved by introducing a symmetry condition for the induced charge density which is assumed to form a surface charge σ^{in}, at $z=\pm\delta$, and n^{in}, at the plane $z=0$. However, we emphasize that the functional behavior of n^{in} in the entire sample is actually unknown. In our ansatz, we determine $n^{in}(x,y,z=0)$ by taking into account a symmetry condition $b=-2$ in Eq. (23). This guarantees the planarity of the total electric field and the charge neutrality of the sample. It is however notable that the shape of the obtained $\mathbf{E}_p$ distribution does not significantly depend on the chosen values $b>0$, $b<0$, or $0<b<1$. It is mainly determined by the spatial distribution of $E_{i,z}$, which represents the underlying physical cause of the surface charge.

The potential electric field distribution $\mathbf{E}_{p,2D}$, obtained from the irrotational contribution of the total electric field $\mathbf{E}_{2D}(x,y)=\rho(J)\mathbf{J}(x,y)$ strongly differs from $\mathbf{E}_p$. Most remarkably, in accordance with the direction of the current flow, $\mathbf{E}_p$ is oriented clockwise, whereas $\mathbf{E}_{p,2D}$ displays areas of counterclockwise orientation in the vicinity of the current domain boundaries. Such behavior is evident in Fig. 7, where the vector field of both potential electric fields, $\mathbf{E}_p$ and $\mathbf{E}_{p,2D}$, are compared. This nonuniform orientation of $\mathbf{E}_{p,2D}$ is related to a much higher charge density in the $z=0$ plane compared to $\mathbf{E}_p$ (see Fig. 8). Since the most important physical origin of the potential electric field is the shear motion of the hopping vortex ensemble, the nonuniform orientational behavior of $\mathbf{E}_{p,2D}$ is in disagreement with the physical expectation of a monotonously changing shear velocity field of the vortices in those regions. Both, a higher degree of homogeneity of the vortex shear motion field as well as less Coulomb energy related to the n^{in} distribution gives evidence that the $\mathbf{E}_p(x,y)$ reconstruction based symmetry arguments of the boundary conditions is physically more realistic than $\mathbf{E}_{p,2D}(x,y)$.

The induced charge density n^{in} is calculated by the equation $\nabla\cdot\mathbf{E}_p=n^{in}/\epsilon_0$. Notice that the boundary conditions on n^{in} are contained in the way, how $\mathbf{E}_p$ is determined. One can observe that, at the plane z=0, n^{in} is not zero. At the current domain boundaries it decays smoothly to zero. Three charge density subdomains are induced in each current domain with uniform current flow. Since the surface charge distribution at the lateral sample edges is two order of magnitude larger than in the bulk, we only display n^{in} at the interior of the thin film. Some features are similar to Brandt's predictions,[14] however, obtained for longitudinal geometry (compare with Fig. 2 of Ref. 16).

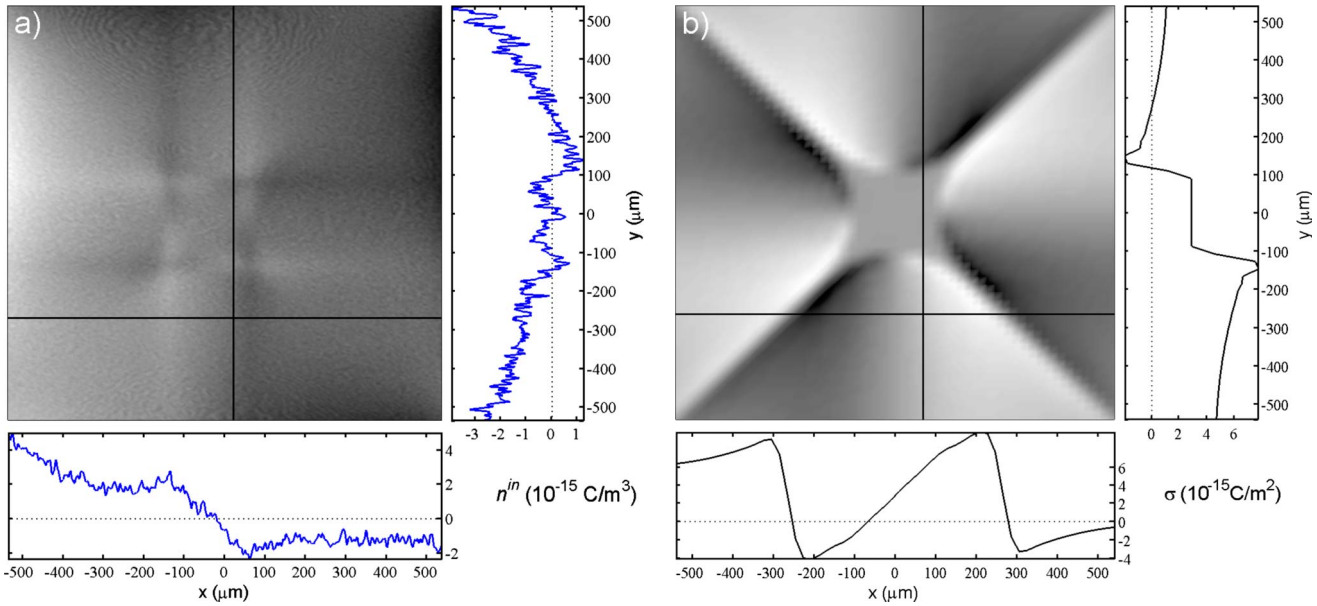

FIG. 8. (Color online) (a) Induced charge density $n^{in}(x,y,z=0)$ obtained from the potential electric field $\mathbf{E}_p$ based on experimental data. (b) Induced surface charge density obtained from the potential electric field $\mathbf{E}_{p,2D}$.

In order to obtain the induced surface charge density in the case of the flux simulation based on the materials law, one can utilize the Helmholtz decomposed $\mathbf{E}_{p,2D}=-\nabla(\nabla\cdot\mathbf{W})$, where the identity $\nabla\cdot\mathbf{W}$ is identified as the scalar potential ϕ. In 2D, it is related to the surface charge density by $\sigma^{in}/\epsilon_0=-\nabla^2\phi$. The induced surface charge density σ^{in} obtained from $\mathbf{E}_{p,2D}$ is quite different from n^{in} (compare panels of Fig. 8). Energetically, σ^{in} presented in panel (b) of Fig. 8 is not favorable compared to n^{in} because the accumulation of charge at the current domain boundaries implies that the pattern of vortex creep must sustain a higher amount of Coulomb energy. Nevertheless, both distributions show no induced charge distribution inside the nonpenetrated area. This represents an important physical test of our method since the Meissner area displays a time-dependent shielding current density without any vortex penetration. Due to the absence of moving vortex cores in the Meissner area, the induced charge density must be zero. In contrast, peaks of n^{in} and σ^{in} are present at the phase boundaries between the Meissner and the flux penetrated areas.

Figure 9 presents the total electric field $\mathbf{E}=\mathbf{E}_i+\mathbf{E}_p$ components. In 2D Fourier space, for the particular case at the $z=0$ plane and under the approximation $k\delta\ll 1$, one yields

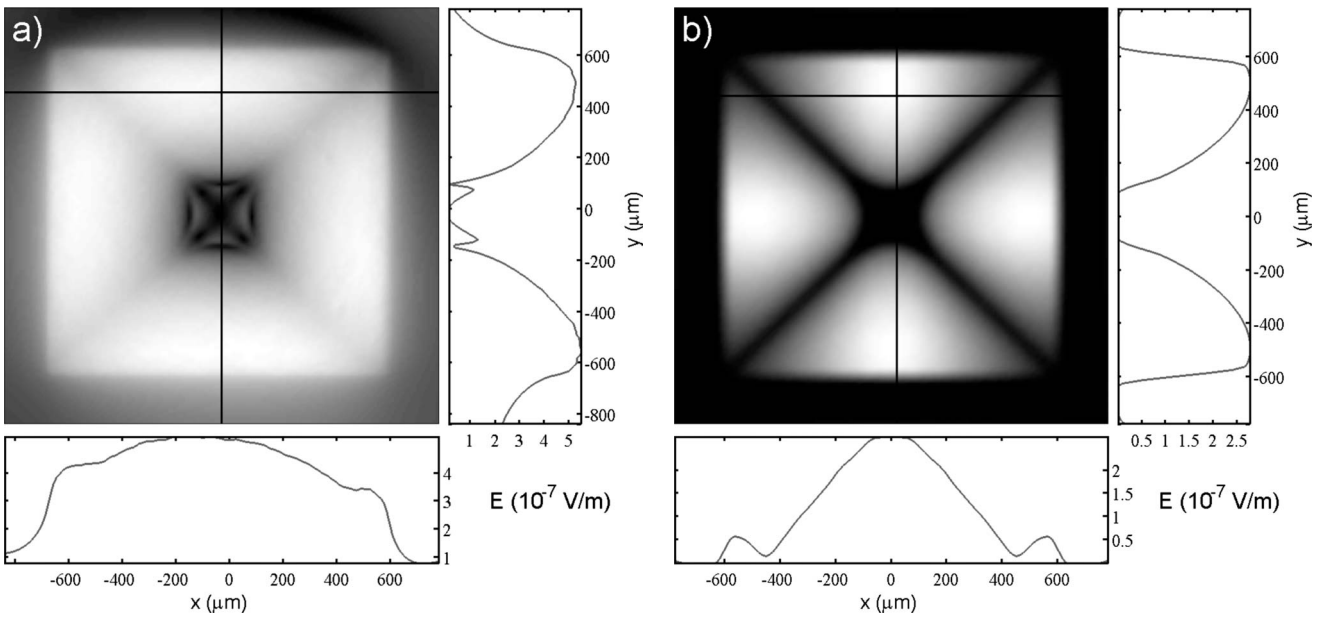

FIG. 9. (a) Total electric field distribution $\mathbf{E}(x,y)=\mathbf{E_i}(x,y)+\mathbf{E_p}(x,y)$ reconstructed from experimental data. (b) Total electric field distribution $\mathbf{E}_{2D}(x,y)=\rho[J(x,y)]\mathbf{J}(x,y)$ in the 2D simulation.

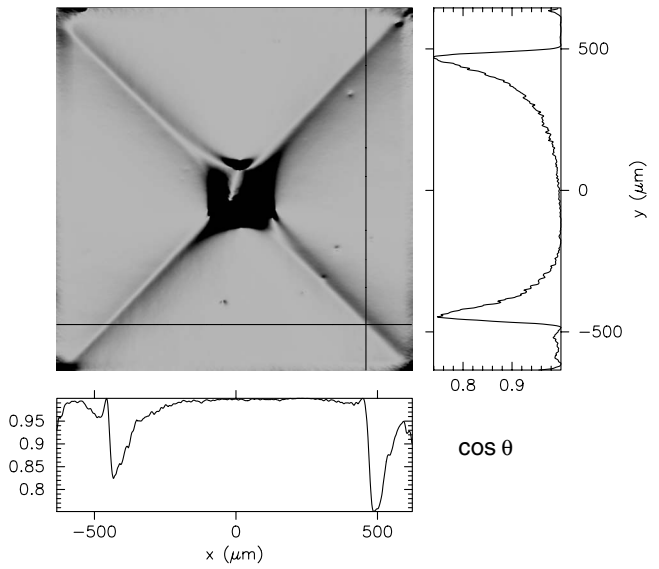

FIG. 10. Relative angle θ between the current density $\mathbf{j}(x,y)$ and the total electric field $\mathbf{E}(x,y)$ represented via $\cos\theta=\mathbf{E}\cdot\mathbf{j}/(|\mathbf{E}||\mathbf{j}|)$. Both $\mathbf{j}(x,y)$ and $\mathbf{E}(x,y)$ are reconstructed from experimental data shown in Fig. 5.

$$\tilde{E}_x = +\mu_0\frac{k_y}{k^3}\dot{\alpha}(k\delta) + \frac{\mu_0}{2}\frac{k_x}{k^3}\dot{\beta}\frac{2b-1}{1-b}(k\delta)^2,$$

$$\tilde{E}_y = -\mu_0\frac{k_x}{k^3}\dot{\alpha}(k\delta) + \frac{\mu_0}{2}\frac{k_y}{k^3}\dot{\beta}\frac{2b-1}{1-b}(k\delta)^2.$$

Comparing $\mathbf{E}$ with the total electric field $\mathbf{E}_{2D}$ obtained by materials law, significant differences are found. The former displays a finite magnitude in the Meissner zone and minimum but finite values at the current domain boundaries. This is in contrast to the material law ansatz, where the magnitude of the electric field $\mathbf{E}_{2D}$ distribution falls drastically to zero at the current domain boundaries and in the Meissner area because of the power-law ansatz for the resistivity. However, it is well known that a temporally varying Meissner current exhibits a finite electric field.

To detail the discussion, Fig. 10 shows the in-plane deviation angle between the total electric field $\mathbf{E}$ and the sheet current $\mathbf{j}$. Inside the current domain boundaries with uniform current flow we find that the total electric field is parallel to the sheet current within the limits of experimental accuracy. In contrast, in the vicinity of the current domain boundaries, large deviation angles up to approx. 41° are present. At this state of the work, we cannot completely rule out that Hall-anglelike features at the current domain boundaries are a result of the chosen approximations, i.e., the assumption of z-independent current density and the boundary conditions for the induced charge density. For example, the presence of lens-shaped remnant Meissner holes at the domain boundary could be the origin of a more pronounced z dependence of the current density at those regions. However, the observation that $\mathbf{E}_p$ and n^{in} exhibit a much more reasonable behavior than $\mathbf{E}_{p,2D}$ and σ^{in} obtained in 2D from an isotropic materials law supports the possibility of an Hall angle at the current domain boundaries. A main argument in favor of a finite Hall angle would be the drastic reduction in the Coulomb energy compared to a flux creep mode, where the total electric field remains strictly parallel to the current and a significant charge density builds up at the current domain boundaries (see, e.g., Ref. 7, Fig. 13).

Usually, significant Hall angles in high-temperature superconductors are mainly observed in the vicinity of T_c and in the flux-flow regime or in transport measurements.[8,24,25] However, we want to emphasize that the detailed structure of a current domain boundary and the mode of flux creep in that complex region is not at all understood until now. The presence of a significant flux creep Hall angle at that region would allow for vortex motions parallel to the domain boundary. In contrast, a creep mode which is dominated by the Lorentz force, a related vortex velocity which is strictly directed perpendicular to the current flow and a resulting isotropic flux creep resistivity has the consequence that the dissipative vortex motion at the domain boundary would be strongly suppressed. This is the underlying reason for the zero total electric field at the domain boundaries in the isotropic approximation. However, dissipative motion in the flux creep state is inevitably related to thermalization process. This supports a homogenization of the dissipated power $\mathbf{j}\cdot\mathbf{E}$ and thus will suppress strong gradients in the total electric field. Indeed, the observation of higher, finite electric field values at the domain boundaries obtained by reconstruction the total electric field by experimental data strongly supports this argument.

Other possible origins of a nonparallel relation between the total electric field $\mathbf{E}$ and the current density $\mathbf{j}$ are an anisotropic crystal structure or flux guiding at anisotropic defects. However, the experimental results are obtained for a purely c-axis-oriented film with a-b twinning on a length scale smaller than the spatial resolution of the magneto-optical method. Moreover, the position and symmetry of the area with finite θ rules out crystallographic or microstructural origins of this effect.

V. CONCLUSIONS

In this paper, we present results on thermally activated flux creep in a superconducting thin film with finite thickness magnetized in a partly penetrated state. Electric field distributions are obtained by reconstruction from experimentally measured time-resolved flux density distributions in a square-shaped YBaCuO thin film and by flux simulations for a infinitesimal-thin-model sample. In the latter case the 2D problem was solved considering a power law for the resistivity with a homogeneous and isotropic critical sheet current J_c. The reconstruction of the potential and induced electric field from experimental data is based on the sheet current approximation for finite but small thickness $d<\lambda$ and assuming a symmetry of the induced charge density which guarantees that the total electric field lies in plane in the quasistationary state. The obtained solution for the potential electric field is more general than the approach of Ref. 7 since it depends only on symmetry arguments and the assumption of an isotropic material law for $\rho(j)$ is not em-

ployed. Our tests that the obtained $\mathbf{E}_p$ does not strongly vary by using different assumptions on the z dependence of n^{in} [parameter b in Eq. (23)] give strong support to the general validity of the solution for $\mathbf{E}_p$.

The obtained $\mathbf{E}_i$ and $\mathbf{E}_p$ distributions for a partially penetrated state deviate significantly from former theoretical works. We find evidence for a finite Hall angle in the vicinity of the domain boundaries, where the flux dynamics is more complex. General qualitative features remain similar when the induced electric field is compared with the corresponding 2D field $\mathbf{E}_{i,2D}$, obtained from the Helmholtz decomposition of the material law. However, drastic differences in the symmetry and orientation are observed for $\mathbf{E}_p$ and $\mathbf{E}_{p,2D}$, respectively, where nonrealistic $\mathbf{E}_{p,2D}(x,y)$ and large induced surface charge are a result of the isotropic materials law.

An important difference of this work to the 2D calculation with infinitesimal thin films[13,14,26] is that the presence of nonzero B_x and B_y components of the magnetic induction at the planes $z \neq 0$ is taken into account. These components generate the $E_{i,z}$ component of the electric field and thus allow for a quasi-3D reconstruction in the thin-film limit in the quasistationary state, if the z dependence of the current density can be (at least to some degree of approximation) disregarded. This method leads to insights into the electric field structure and possible inhomogeneous modes of vortex creep at special locations such as domain boundaries which are beyond the approximation of an isotropic uniform materials law. Our results give evidence that such an isotropic uniform materials law which is obtained from macroscopic transport measurements under stationary conditions cannot be applied with restrictions to the local magnetization decay of a superconductor due to flux creep. Important consequences are expected for the flux creep nearby inhomogeneties, where additional current domain boundaries and local inhomogeneities of the electric field distribution evolve.

ACKNOWLEDGMENTS

This research was supported by a Grant from the GIF, the German-Israeli Foundation for Scientific Research and Development. C. Romero-Salazar acknowledges support from DAAD and repatriation Conacyt support under Grant No. 103655. O.A. Hernández-Flores acknowledges the hospitality of the Institut für Materialphysik, Göttingen. Helpful discussions with E.H. Brandt and G.P. Mikitik are gratefully acknowledged.

APPENDIX

Evaluation of the function ζ

The calculation of $\tilde{E}_{i,z}$ requires the integration of

$$\zeta = \int_{-\infty}^{+\infty} dz'^{-k|z-z'|}\{e^{-k|z'-\delta|} - e^{-k|z'+\delta|}\}.$$

By definition, the absolute value of the integral ζ can be written as follows:

$$\zeta = \zeta_1 + \zeta_2,$$

$$= \int_{-\infty}^{z} dz'^{-k(z-z')}\{e^{-k|z'-\delta|} - e^{-k|z'+\delta|}\} + \int_{z}^{+\infty} dz'^{+k(z-z')}\{e^{-k|z'-\delta|} - e^{-k|z'+\delta|}\}.$$

We are interested on the electric field inside the superconductor, therefore, we will assume that $z \in [-\delta, \delta]$. With this condition the integral ζ_1 is given by

$$\zeta_1 = \int_{-\infty}^{-\delta} dz'^{-k(z-z')}\{e^{+k(z'-\delta)} - e^{+k(z'+\delta)}\} + \int_{-\delta}^{z} dz'^{-k(z-z')}\{e^{+k(z'-\delta)} - e^{-k(z'+\delta)}\},$$

$$= -\frac{1}{k}e^{-k(z+\delta)}\sinh(k\delta)e^{-k\delta} + e^{-k(z+\delta)}\left\{-(z+\delta) + \frac{e^{+2kz}}{2k} - \frac{e^{-2k\delta}}{2k}\right\},$$

and ζ_2 by

$$\zeta_2 = \int_{+\delta}^{+\infty} dz'^{+k(z-z')}\{e^{-k(z'-\delta)} - e^{-k(z'+\delta)}\} + \int_{z}^{+\delta} dz'^{+k(z-z')}\{e^{+k(z'-\delta)} - e^{-k(z'+\delta)}\},$$

$$= +\frac{1}{k}e^{+k(z-\delta)}\sinh(k\delta)e^{-k\delta} + e^{+k(z-\delta)}\left\{(\delta - z) - \frac{e^{-2kz}}{2k} + \frac{e^{-2k\delta}}{2k}\right\}.$$

Adding ζ_1 and ζ_2 we obtain

$$\zeta = \frac{e^{-k\delta}}{k}\{D\sinh(kz) - 2kz\cosh(kz)\},$$

where

$$D = 2e^{-k\delta}\sinh(k\delta) + 1 + 2k\delta + e^{-2k\delta} = 2k\delta + 2.$$

*Current address: Escuela de Ciencias, Universidad Autónoma "Benito Juárez" de Oaxaca, Av. Universidad s/n, Ex Hacienda Cinco Señores, Oaxaca de Juárez, Oaxaca CP 68120 México.

†Author to whom correspondence should be addressed; jooss@ump.gwdg.de

[1] D. C. Larbalestier, A. Gurevich, D. M. Feldmann, and A. Polyanskii, Nature (London) **414**, 368 (2001).

[2] J. Bardeen and M. J. Stephen, Phys. Rev. **140**, A1197 (1965).

[3] M. W. Coffey and Z. Hao, Phys. Rev. B **44**, 5230 (1991).

[4] X. L. Zhou, Progress Electromagn. Res., PIER **65**, 93 (2006).

[5] F. London, *Superfluids* (Wiley, New York, 1950), Vol. 1, p. 55.

[6] P. Lipavsky, J. Kolacek, K. Morawetz, and E. H. Brandt, Phys. Rev. B **65**, 144511 (2002).

[7] Ch. Jooss and V. Born, Phys. Rev. B **73**, 094508 (2006).

[8] G. Blatter, M. V. Feigel'man, V. B. Geshkenbein, A. I. Larkin, and V. M. Vinokur, Rev. Mod. Phys. **66**, 1125 (1994).

[9] C. Dekker, P. J. M. Wöltgens, R. H. Koch, B. W. Hussey, and A. Gupta, Phys. Rev. Lett. **69**, 2717 (1992).

[10] A. D. Caplin, L. F. Cohen, G. K. Perkins, and A. A. Zhukov, Supercond. Sci. Technol. **7**, 412 (1994).

[11] M. Friesen and A. Gurevich, Phys. Rev. B **63**, 064521 (2001).

[12] A. Gurevich and M. Friesen, Phys. Rev. B **62**, 4004 (2000).

[13] E. H. Brandt, Phys. Rev. Lett. **74**, 3025 (1995).

[14] E. H. Brandt, Phys. Rev. B **52**, 15442 (1995).

[15] A. Gurevich and E. H. Brandt, Phys. Rev. Lett. **73**, 178 (1994).

[16] E. H. Brandt, Phys. Rev. Lett. **76**, 4030 (1996).

[17] D. Giller, Y. Abulafia, R. Prozorov, Y. Wolfus, A. Shaulov, and Y. Yeshurun, Phys. Rev. B **57**, R14080 (1998).

[18] R. Warthmann, J. Albrecht, H. Kronmüller, and Ch. Jooss, Phys. Rev. B **62**, 15226 (2000).

[19] E. H. Brandt, Rep. Prog. Phys. **58**, 1465 (1995).

[20] Ch. Jooss, J. Albrecht, H. Kuhn, S. Leonhardt, and H. Kronmüller, Rep. Prog. Phys. **65**, 651 (2002), and references therein.

[21] J. Bentner, D. Babic, C. Surgers, and C. Strunk, Phys. Rev. B **70**, 184516 (2004).

[22] Y. F. Gui and W. B. Dou, Progress Electromagn. Res., PIER **69**, 287 (2007).

[23] Ch. Jooss, R. Warthmann, A. Forkl, and H. Kronmueller, Physica C **299**, 215 (1998).

[24] R. P. Huebener, *Magnetic Flux Structures in Superconductors*, 2nd ed. (Springer-Verlag, Germany, 1979).

[25] B. König and H. Kirchner, Phys. Status Solidi A **28**, 467 (1975).

[26] E. H. Brandt, Phys. Rev. B **54**, 4246 (1996).